Synergistic antibacterial activity of physical-chemical multi-mechanism by TiO₂ nanorod arrays for safe biofilm eradication on implant

Xiangyu Zhang[a,b,c,*], Guannan Zhang[a], Maozhou Chai[b], Xiaohong Yao[a], Weiyi Chen[b], Paul K. Chu[d,**]

[a] *Laboratory of Biomaterial Surfaces & Interfaces, Institute of New Carbon Materials, Taiyuan University of Technology, Taiyuan, 030024, China*
[b] *College of Biomedical Engineering, Taiyuan University of Technology, Taiyuan, 030024, China*
[c] *Second Hospital of Shanxi Medical University, Taiyuan, 030024, China*
[d] *Department of Physics, Department of Materials Science and Engineering, Department of Biomedical Engineering, City University of Hong Kong, Tat Chee Avenue, Kowloon, Hong Kong, China*

ARTICLE INFO

ABSTRACT

Treatment of implant-associated infection is becoming more challenging, especially when bacterial biofilms form on the surface of the implants. Developing multi-mechanism antibacterial methods to combat bacterial biofilm infections by the synergistic effects are superior to those based on single modality due to avoiding the adverse effects arising from the latter. In this work, TiO₂ nanorod arrays in combination with irradiation with 808 near-infrared (NIR) light are proven to eradicate single specie biofilms by combining photothermal therapy, photo-dynamic therapy, and physical killing of bacteria. The TiO₂ nanorod arrays possess efficient photothermal conversion ability and produce a small amount of reactive oxygen species (ROS). Physiologically, the combined actions of hyperthermia, ROS, and puncturing by nanorods give rise to excellent antibacterial properties on titanium requiring irradiation for only 15 min as demonstrated by our experiments conducted *in vitro* and *in vivo*. More importantly, bone biofilm infection is successfully treated efficiently by the synergistic antibacterial effects and at the same time, the TiO₂ nanorod arrays improve the new bone formation around implants. In this pro-tocol, besides the biocompatible TiO₂ nanorod arrays, an extra photosensitizer is not needed and no other ions would be released. Our findings reveal a rapid bacteria-killing method based on the multiple synergetic anti-bacterial modalities with high biosafety that can be implemented *in vivo* and obviate the need for a second operation. The concept and antibacterial system described here have large clinical potential in orthopedic and dental applications.

1. Introduction

The demand for orthopedic and dental implants is increasing as people live longer and the quality of people's life continues to improve worldwide. Implant-related infections induced by bacteria, especially bacterial biofilms, are one of the major causes of implant failure [1]. The abuse of antibiotics has led to multidrug-resistant bacteria, which is rendering conventional treatment ineffective. In serious cases, a second surgery to remove the infected implants is necessary consequently in-creasing health cost and patient trauma [2]. Therefore, there is much research focus in endowing the surface of implants with the self-anti-bacterial ability. Fabrication of such surfaces fall into two categories,

chemical methods based on the release of antimicrobial agents such as inorganic metal ions (Ag⁺, Cu²⁺, Zn²⁺, Mg²⁺, etc.) and organic anti-microbial agents and antibiotics [3–7] as well as physical approaches that produce special surface structures [8–11] that resist bacteria co-lonization but support cell adhesion and proliferation. Both techniques have advantages and drawbacks. With regard to chemical methods, incorporation of metal ions can endow biomaterials with excellent antibacterial activity but may produce adverse side effects [10] and organic antimicrobial agents tend to have weak antibacterial activity and poor long-term performance [7]. In fact, overuse of antibiotics has led to antimicrobial resistance and super bacteria [12]. In contrast, physical surface structures are safer and more sustainable. Since the

discovery that the cicada wing surfaces can kill bacteria based on the rupturing mechanism by the nanoscale pillar arrays [13], this mechanism has attracted much interest but there are limitations. For example, cicada wings only kill gram negative bacteria effectively but not gram positive bacteria [14]. Nanostructured black silicon can kill *S. aureus* and *P. aeruginosa* in very short time in a nutrient deficient environment but in a nutrient rich environment, the bacteria could survive up to 6 h [8]. It has also been reported that nanostructured bactericidal surfaces can only kill attached microbes [15] and in general, a nanostructured surface is inefficient and may not prevent post-surgical infection on implants effectively.

Recently, phototherapy including photodynamic antibacterial (PDA) and photothermal antibacterial (PTA) has received extensive attention due to the high antibacterial efficiency [16]. PDA is based on the principle that photocatalytic materials can generate reactive oxygen species (ROS) upon visible or near-infrared (NIR) light to oxidize phospholipids and proteins of bacteria, while an excess amount of ROS may cause cytotoxic effects [17]. PTA relies on photothermal agents that convert NIR light into local heating to kill bacteria, while the major problem of this type of therapy is that it is difficult to kill bacteria at the temperature that can be tolerated by the human body [18]. Interestingly, the synergistic effects of hyperthermia and ROS which both are in the safe range can kill bacteria rapidly and efficiently. Therefore, the combination of PTA with PDA to prevent bacterial infection has attracted more attention and in fact shown promising antibacterial effects [19,20]. However, the long-term safety of the common photocatalytic and photothermal materials such as carbon-based nanomaterials [21], black phosphorus [22], red phosphorus [19], MoS_2 [23–25], gold nanoparticles [26], and copper sulfide [27] remains to be seen *in vivo*.

TiO_2 has unique characteristics such as excellent biocompatibility, mechanical properties, and corrosion resistance [28] in addition to the photocatalytic capability. However, the band gap of TiO_2 is 3.2 eV thereby requiring activation by ultraviolet (UV) light which greatly limits practical applications [29] and *in vivo* investigation on bacteria killing *in vivo* by pure TiO_2 as the photocatalytic or photothermal materials is quite rare.

In this study, amultiple synergetic antibacterial modality based on the combining photothermal therapy, photodynamic therapy and physical killing by TiO_2 nanostructures under the irradiation of 808 nm NIR light is proposed. TiO_2 nanorod arrays are demonstrated to be an efficient photosensitizer in antibacterial applications by combining irradiation with 808 nm NIR light and physical killing by nanorod arrays. The TiO_2 nanorod arrays are hydrothermally prepared on Ti [30–32] and the surface temperature of the TiO_2 nanorod arrays rise to a range that the human body can withstand for a short period of time during irradiation with NIR light. The combined actions of generated hyperthermia, ROS, and puncturing by nanorods produce superior antibacterial and anti-biofilm activities *in vitro* and *in vivo*. At the same time, the nanorod arrays improve cell adhesion, proliferation, and osteogenic differentiation consequently accelerating bone tissue regeneration and irradiation with 808 nm NIR light does not impair the growth of osteoblasts.

2. Experimental

2.1. Preparation of nanorod arrays and sample characterization

The TiO_2 nanostructures were prepared by a hydrothermal reaction with a polished Ti metal foil in a sodium hydroxide (NaOH) solution and the ordered TiO_2 nanorod arrays were fabricated by ion exchange in hydrochloric acid followed by annealing in air. The Ti foil specimens (2.5×3.0 cm^2) were ultrasonically cleaned with acetone, alcohol, and distilled water for 5 min sequentially. A piece of the Ti foil was placed against the wall of a 40 mL Teflon-lined stainless steel autoclave filled with 30 mL of 1 M NaOH and the sealed autoclave was put in an electric oven at 220 °C for 1, 2, 3, and 4 h.The samples covered with $Na_2Ti_2O_5$

nanostructures were immersed in 1 M HCl for 30 min to replace Na^+ with H^+ to produce the $H_2Ti_2O_5 \cdot H_2O$ nanostructures. The specimens were removed from HCl, rinsed with water and ethanol, and dried under ambient conditions. The TiO_2 nanostructures were prepared by heating the $H_2Ti_2O_5 \cdot H_2O$ at 450 °C in a muffle furnace for 2 h and the samples were labeled NS1, NS2, NS3, and NS4 according to hydrothermal time of 1, 2, 3, and 4 h, respectively. The samples were characterized by field emission scanning electron microscopy (FE-SEM, JSM-7001 F, JEOL), atomic force microscopy (AFM, XE-100, Park Systems) and high-resolution transmission electron microscopy (HR-TEM, JEM-2100F, JEOL). The phase constituents of the nanostructures were analyzed using X-ray diffraction(XRD, Rigaku Dmax-3C, Cu Kα radiation). The chemical states were determined by X-ray photoelectron spectroscopy (XPS, K-Alpha, Thermo Fisher Scientific) with Al Kα radiation. The surface hydrophilicity of the polished Ti and nanostructures was determined by the sessile drop method on the Rame'-Hart instrument (USA) at room temperature. A droplet of water was put onto the dry surface and the contact angle was calculated by a circle segment function of the DSA 1.8 software. The UV–vis–NIR absorption and reflectance spectra were acquired on the 46 solidspec-3700 spectrophotometer UV-2 (Shimadu, Japan) between 300 and 900 nm.

2.2. Photothermal effects

The Ti and TiO_2 nanostructures (NS1, NS2, NS3 and NS4) (1.0×1.0 cm^2) were immersed in 1 mL of phosphate buffer saline (PBS) and then exposed to 808 nm NIR light (0.6, 0.8, 1.0 and 1.2 W cm^{-2}) for 15 min. The temperature of the samples was determined by a thermal camera (FLIR C2, USA) at an interval of 1 min. After irradiation, the cooling temperature was recorded every minute until the temperature was near room temperature.

2.3. Detection of $^1O_2$ and $\cdot OH$

$^1O_2$ and $\cdot OH$ generation from the TiO_2 nanostructures upon 808 nm NIR light (1.0 W cm^{-2}) was detected to evaluate the photodynamic properties. The pure Ti was used as the controls. The samples were immersed in 3 mL of 1,3-diphenylisobenzofuran (DPBF) and methyl violet, respectively and after irradiation with NIR light for 15 min, the optical densities of the solutions were determined by UV–vis spectrophotometry.

2.4. In vitro antibacterial properties

The antibacterial activity of the sterilized samples was evaluated against Gram-negative (*E. coli*, ATCC10536) and Gram-positive (*S. aureus*, ATCC 25923) bacteria. The broth for culturing the bacteria was made by dissolving 5.0 g flesh extract, 5.0 g NaCl and 10.0 g peptone into 1000 mL of distilled water with the pH adjusted to 7.0–7.2.After 12 h culture in a 37 °C incubator, bacterial suspensions were then centrifuged, washed and resuspended in 0.9% physiological saline solution for further use. Each bacterial suspension was independently adjusted by measuring its optical density at 600 nm. The sterilized samples were placed in a 24-well plate and 1 mL of the bacterial suspension at a concentration of 1×10^7 CFU/mL ($OD_{600} = 0.5$ for *S. aureus* and $OD_{600} = 1.0$ for *E. coli*) in exponential growth phase was added to each sample. The samples were irradiated with 808 nm NIR light with different power densities of 0.6, 0.8, 1.0, and 1.2 W cm^{-2} for 15 min. After the treatment, the samples were rinsed with PBS to detach the bacteria from the surfaces. Meanwhile, the bacteria suspension was diluted 100 times and 80 μL of the diluted bacteria solution were spread on agar plates for CFU analysis. After incubation at 37 °C for 24 h, the bacterial colonies were counted and the antibacterial ratio was calculated by the following formula: $R = [(\lambda 0 - \lambda t / \lambda 0] \times 100\%$, in which R is the antibacterial rate (%), $\lambda 0$ is the average number of viable bacteria on control sample and λt is the average number of viable

bacteria on Ti, NS1, NS2, NS3 and NS4 under NIR light irradiation. The Ti group without irradiation constituted the control.

After irradiated with 808 nm NIR light of 0.8 W cm^{-2} for 15 min, the adherent bacteria on Ti, NS1, NS2, NS3, and NS4 were fixed with 2.5% glutaraldehyde for 2 h, dehydrated with a series of graded ethanol (20–100%), freeze dried, and sputter-coated with platinum for SEM observation.

2.5. In vitro antibiofilm assay

E. coli and S. aureus were used to evaluate the antibiofilm activity. 2 mL of the bacterial solution at a concentration of 1×10^7 CFU/mL were cultivated on the samples for 48 h to form biofilms. The culture medium was changed every 12 h and the samples were irradiated with the 808 nm laser (0.8W cm^{-2}) for 15 min. The biofilms were stained with mixed dye (LIVE/DEAD BacLight bacteria viability kits) in darkness for 15 min, washed with PBS. Then, four regions of 1000 nm × 1000 nm were stochastically photographed by confocal scanning laser microscope (CLSM, C2 Plus, Nikon) with a magnification of 100 times to live/dead assay of biofilm. The resolution of CLSM scanning is 10 μm.

In fluorescent staining, the samples with biofilm were stained with acridine orange, and four regions of 1000 nm × 1000 nm were stochastically photographed by confocal scanning laser microscope (CLSM, C2 Plus, Nikon) with a magnification of 100 times.

2.6. Bacterial membrane permeability assay

The permeability of bacterial cell membrane on the surface of Ti and NS4 was investigated by Ortho-nitrophenyl-β-galactoside (ONPG). After treatment with 808 nm light (0.8 W cm^{-2} for 15 min) or without light irradiation, the samples were analyzed by ONPG assay kit. The supernatant absorbance was recorded at 420 nm.

2.7. Protein leakage

Ti and NS4 were placed in 1 mL bacterial suspension (5×10^7 CFU/mL). After treatment with 808 nm light (0.8 W cm^{-2}) or without light irradiation for 15min. The bacterial suspension was centrifuged at 5000 rpm for 10 min at 4 °C. Following that, the amount of protein leaked into the supernatant was determined by an assay kit (cat# P0009; Beyotime).

2.8. Biocompatibility assessment

The osteoblasts (MC3T3-E1, Shanghai Chinese Academy of Sciences, Catalog number: GNM15) were cultured with Minimum Essential Medium Alpha Medium (α-MEM, Gibco, America) supplemented with 10% of fetal bovine serum (FBS, Sijiqing, China) and 1% of antibiotic–antimycotic solution consisting of 100 units/mL penicillin and 100 mg/mL streptomycin at 37 °C in a humidified incubator filled with 5% CO_2 and 95% air. Pure Ti was used as the control. The osteoblasts were incubated on the Ti and TiO_2 nanostructures with a density of 2×10^4 cells/cm^2 with the normal complete medium and the culture medium was refreshed every other day. The cell viability was evaluated quantitatively by the 3-(4,5-dimethylthiazol-2-yl)-2,5-diphenyl tetrazolium bromide (MTT) assay. After incubation for 1, 3, and 5 days on the samples, the cell-adhered specimens were washed with PBS and 1 mL of MTT solution (5 mg/mL) were added and incubated at 37 °C for 4 h. 1 mL of dimethyl sulfoxide (DMSO, Sigma, USA) was used to dissolve the formazan. 100 μL of the dissolved formazan from each well were transferred to a 96-well plate to measure the optical density (OD) on a microplate reader (Infinite F50, TECAN) at a wavelength of 490 nm. Fluorescent staining was performed to observe the cell morphology on the samples. After culturing for 24 h, the cells were fixed with 4% paraformaldehyde for 30 min, stained with fluorescein is

othiocyanate (FITC)-phalloidin (Sigma, USA) in darkness for 1 h, and counter stained with 4,6-diamidino-2-phenylindole (DAPI; Sigma, USA) in darkness for 20 min. The fluorescent images were captured under a CLSM. Furthermore, to explore the safety of the nanostructures with the 808 nm light irradiation, a control group was conducted after cells exposed to light for 15 min. After culturing for 24 and 48 h, the fluorescent images were captured.

2.9. Intracellular Alkaline Phosphatase (ALP) activity, collagen secretion, and extracellular matrix (ECM) mineralization

After culturing for 4 and 7 days, the MC3T3-E1 cells were lysed in the PBS solution with 1% Triton X-100 and incubated at 37 °C for 30 min. The ALP activity was determined by the bicinchoninic acid protein assay kit (cat# P0321; Beyotime, China) and type I collagen secretion of Ti and TiO_2 nanostructures was quantitatively tested by Direct Red (Sigma, America). After osteogenic induction for 7 and 14 days, the MC3T3-E1 cells were fixed with PFA and stained with Direct Red, washed with acetic acid, and immersed in a fading solution to elute the stain. Finally, the OD was measured at 570 nm. Extracellular matrix (ECM) mineralization was tested by Alizarin Red (aladdin, China). Similarly, after culturing for 7 and 14 days, the MC3T3-E1 cells were fixed in ethanol and stained with Alizarin Red S for ECM mineralization. The mineralized nodules were eluted with hexadecyl pyridinium chloride and the OD of the solution was measured at 570 nm.

2.10. Osteogenic-related gene expression

The MC3T3-E1 cells were harvested to assess gene expression after culturing for 7 days. The total RNA was isolated from OBs for the real-time quantitative polymerase chain reaction (RT-qPCR) using Eastep® Super Total RNA Extraction Kit (Promega). The complementary DNA was synthesized from total RNA using the PrimeScript™ RT reagent Kit with gDNA Eraser (Takara) and expressions of the runt-related transcription factor 2 (Runx2) and osteocalcin (OCN) were assayed by the StepOne RT-qPCR System (Applied Biosystems) with the TB Green™ Premix Ex Taq™ II (Takara). The primer sequences used in RT-qPCR are presented in Table S1. The comparative CT (ΔΔCT) method was used to calculate the relative expression of the target genes compared with the control negative group (osteoblasts seeded on the blank culture plate and cultured with the normal complete medium) after calibrating with the GAPDH RNA content.

2.11. Animal experiments

Male Kunming mice (300–320 g body weight) were purchased from Shanxi Medical University. A mouse subcutaneous infection model was firstly adopted and the animal procedures were conducted under the guidance of the Institutional Animal Care. Both the conventional antibacterial assay and antibiofilm assay in vivo against S. aureus were performed. Twenty-four mice were individually raised in cages for 3 days and randomly divided into four groups (six in each group): Ti + bacteria solution, NS4 + bacteria solution, Ti + biofilm and NS4 + biofilm. The mice were anesthetized using four percent pentobarbital (0.4 mL per 100 g) by intraperitoneal injection. The induction time was 10 min and anesthesia duration was about 80 min. For the antibacterial assay, the samples 10 mm long and 5 mm wide were soaked in 50 μL of S. aureus (1×10^7 CFU/mL) for 1 h and then implanted into the subcutaneous tissue on the back of the mice.

For the antibiofilm assay, 2 mLof the bacterial solution (10^7 CFU/mL) were cultivated on the samples for 48 h to form biofilms and the same size samples with biofilms were implanted into the subcutaneous tissue on the back of the mice. The wound site of the mouse was irradiated with 808 nm NIR light for 15 min with the maximum temperature kept below 50 °C. After feeding for 2 days, half of the mice were euthanized. The infected tissues from each group were obtained to

seed on a standard agar culture plate to investigate the antibacterial properties by spread plate analysis. The tissues attached to the samples were harvested and soaked in 4% paraformaldehyde for fixing, washed with PBS, dehydrated in gradient ethanol solutions (75, 85, 90, 95 and 100%), filtered with xylene and paraffin, and embedding with paraffin. After staining with H&E and Giemsa, the histological pictures were obtained on an optical microscope (Leica RM2016, Leica Microsystems, Germany). The other mice were fed for 14 days and the sections of the infected site were subjected to H&E staining.

For *in vivo* osteogenic activity assay, twelve mice were individually raised in cages for 3 days and randomly divided into two groups (six in each group): Ti + biofilm and NS4 + biofilm. The mice were first anesthetized with 10% chloral hydrate, then a narrow hole with a diameter of 1.5 mm was created at the tibia using a surgical drill. Following that, the implants with *S. aureus* biofilm were gently inserted into the holes, and then the soft tissue and skin were sutured. At the first postoperative day, the implantation site was irradiated with 808 nm laser as the same parameters of subcutaneous experiments *in vivo*. After 2 days feeding, three mice were sacrificed in each group and the implants were removed. The antibacterial properties *in vivo* were evaluated by spread plate and staining of soft tissue. The remaining mice were sacrificed for the evaluation of the osseointegration.

Micro-CT (viva-CT 40, Scanco Medical AG, Bassersdorf, Switzerland) was performed to observe the new bone formation on the implants. The resolution of micro-CT scanning is 10 µm. Different thresholding procedure was used to distinguish bone and titanium implant ($\sigma = 0.8$, support = 1, threshold for bone = 35, and threshold for implant = 211). The scanning images were reconstructed to obtain 3D images and quantitate the new bone volume (BV), percentage of bone volume to tissue volume (%, BV/TV). Safranin-O/Fast Green staining and Methylene Blue−Acid Fuchsin staining were also used to assess the new formed bone on the surface of the implants.

2.12. Statistical analysis

All the experiments were performed in triplicate and the experimental data were expressed as mean ± standard deviation using SPSS 14.0 software. One-way ANOVA followed by Student-Newman-Keuls post hoc test was employed to determine the level of significance. In the statistical evaluation, *$p < 0.05$, **$p < 0.01$ and ***$p < 0.001$ were regarded as significant, highly significant, and extremely significant, respectively.

3. Results

3.1. Sample characterization

The morphology of the TiO$_2$ nanostructures can be tuned by varying the time of the hydrothermal treatment [33]. Four TiO$_2$ nanostructures were fabricated on Ti for different reaction time of 1, 2, 3, and 4 h and the corresponding nanostructures are designated as NS1, NS2, NS3, and NS4, respectively. The SEM images in Fig. 1 and Figure S 1 reveal that NS1 has a homogeneous 2D nanoleaf pattern. The leaves have a micro size laterally and nanosize in thickness. When the hydrothermal time is increased to 2 h (NS2), the lateral dimensions of the leaves decrease but the thickness increases. As the hydrothermal time is increased further, the nanoleaf structure morphs into a nanorod-like morphology and some sheet-like structures still exist after 3 h (NS3). A nanorod structure with a diameter of 40–50 nm and length of about 1 µm is obtained after 4 h (NS4). Fig. 1 b shows the TEM image of the nanorod in NS4 with a diameter of 45 nm consistent with SEM. In addition to the phase of TiO$_2$, the residual H$_2$Ti$_2$O$_5$ is also observed [33]. XPS is carried out to determine the chemical states and as shown in Fig. 1 c, Ti and O are present and Ti is in the form of Ti^{4+}. Fig. 1 d shows the XRD patterns of the nanostructures. The main phases are TiO$_2$ and pure Ti, and the TiO$_2$ phase is mainly composed of anatase. No feature peaks of H$_2$Ti$_2$O$_5$

phase are detected due to the low concentration in the nanostructures. As shown in Figure S 2 and Fig. 1 e, the root-mean-square roughness increases with hydrothermal time. The water contact angles on the Ti and TiO$_2$ nanostructures are presented in Fig. 1 f. The contact angles of NS1, NS2, NS3, and NS4 are less than 3° indicating that the TiO$_2$ nanostructures improves the hydrophilicity of Ti. To investigate the effect of NIR light irradiation on the wettability, the contact angles of Ti and NS4 were measured after light exposure for 1, 2 and 3 h. As shown in Figure S 3, there is no significant difference in the contact angles, suggesting that the irradiation of NIR light have no effect on the hydrophilicity.

3.2. Light-to-heat conversion

To evaluate the photothermal conversion ability, the Ti and nanostructured samples were irradiated with an 808 nm NIR laser in PBS with different power densities (0.6, 0.8, 1.0 and 1.2 W cm^{-2}). As shown in Figure S 4 and Fig. 2 b, the temperature of the samples depends on the light power and illumination time [34,35]. In general, the temperature elevation increases with power as well as irradiation time finally reaching a plateau. The nanostructures also have large effects on the surface temperature. Ti possesses a certain photothermal conversion capacity and the highest temperature upon irradiation with the different power densities is 39.7, 50.0, 52.4, and 56.4 °C respectively. Under the same irradiation conditions, the temperature of NS1, NS2, NS3, and NS4 is higher than that of Ti. The temperature increase of NS1 is slightly less than that of the others but no appreciable difference is found among NS2, NS3, and NS4. The maximum stable temperature of NS1, NS2, NS3, and NS4 for different power densities is 48.2, 56.5, 59.5, and 64.1 °C, respectively. The surface temperature of the samples irradiated with NIR light in air with a power of 0.8 W cm^{-2} is investigated and shown in Fig. 2 a. The samples reach the temperature after 5 min and the temperature of Ti, NS1, NS2, NS3, and NS4 remains stable at 93.7, 113.6, 138.3, 146.3, and 152.1 °C, respectively, demonstrating that the TiO$_2$ nanostructures possess better photothermal conversion ability. As shown in Fig. 2 c, with or without NIR light irradiation, the temperature exhibits a stable on–off effect and the same phenomenon can be observed in subsequent cycles indicating the excellent photothermal stability of the nanostructures. The cooling curves after turning off the light are shown in Figure S 5 and Fig. 2 d which show that the surface temperature of all the samples diminishes rapidly reduced within 1 min and then gradually.

The optical properties play a major role in the photothermal response and the UV–Vis–NIR spectra were acquired from Ti and NS4. As shown in Figure S 6a, NS4 shows strong absorption in the UV region because of the TiO$_2$ nanostructures doped with little H$_2$Ti$_2$O$_5$. Compared to Ti, NS4 exhibits obviously enhanced absorption in the visible to NIR wavelengths. The reflectivity and absorptivity of Ti and NS4 at 808 nm are shown in Figure S 6b. NS4 has higher absorption and lower reflectivity than Ti corroborating the excellent photothermal conversion efficiency of NS4. In addition to the intrinsic optical properties of TiO$_2$, we believe that the nanostructures make major contributions to the photothermal effects [36]. The nanostructures can improve the heat-transfer performance [37,38] thus facilitating photothermal conversion. Moreover, the heat generated in photocatalysis may also contribute to the rising temperature but the process may produce very little heat due to weak photocatalysis of TiO$_2$ when irradiated with 808 NIR light.

3.3. ·OH and ^{1}O$_2$ Detection

Generally, TiO$_2$ is not considered to possess NIR light photocatalytic activity [28,29]. However, the TiO$_2$ nanostructures doped with little H$_2$Ti$_2$O$_5$ can produce a trace amount of ROS when irradiated with NIR light. To investigate the photocatalytic effects of the TiO$_2$ nanostructures, experiments using methyl violet and DPBF were performed
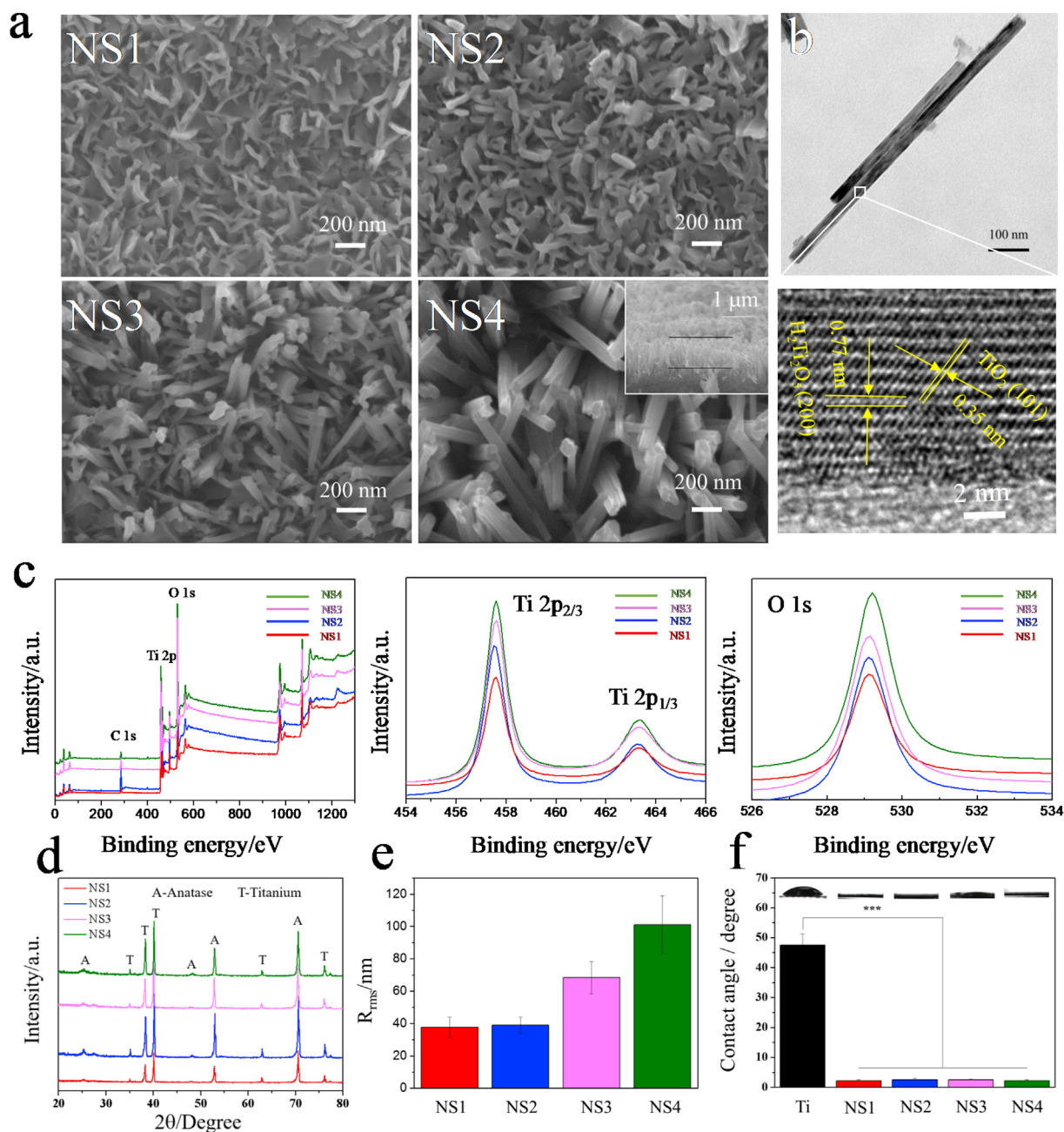
Fig. 1. (a) SEM images of NS1, NS2, NS3, and NS4 with the insets showing the corresponding cross-sectional images; (b) TEM image of the nanorod separated from NS4; (c) XPS survey spectrum and high-resolution spectra of Ti 2p and O1s of the TiO_2 nanostructures; (d) XRD patterns of the TiO_2 nanostructures; (e) Root-mean-square roughness values of NS1, NS2, NS3, and NS4 determined by AFM; (f) Contact angles on the TiO_2 nanostructures.

under irradiation with 808 nm NIR light at 0.8 W cm^{-2}. Methyl violet and DPBF can respectively react with ·OH and $^1O_2$ to reduce the absorption intensity at about 580 and 420 nm consequently producing ·OH and $^1O_2$ during light irradiation as reflected by the decreased absorbance [39,40]. As shown in Fig. 2 e-h, after irradiation for 15 min, the intensity of the absorption peaks of the TiO_2 nanostructures is lower than that of pure Ti, indicating that the TiO_2 nanostructures under irradiation produce a certain amount of ·OH and $^1O_2$. However, there is no significant difference among NS1, NS2, NS3, and NS4. The nanostructures might adsorb organic solution, thus reducing the absorption intensity. We further tested the yield of ROS produced by Ti, NS4 and $Na_2Ti_2O_5$ nanorod arrays at different illumination time, respectively. $Na_2Ti_2O_5$ nanorod arrays were prepared by the hydrothermal treatment of Ti, and NS4 was obtained after acid pickling and calcination. Therefore, $Na_2Ti_2O_5$ nanorod arrays (Figure S 7) have the same

structure as NS4. Apparently, the decreased absorption intensity produced by $Na_2Ti_2O_5$ nanorod arrays is significantly lower than that of produced by NS4, suggesting that a certain amount of ·OH and $^1O_2$ was generated by TiO_2 nanostructures under the irradiation of 808 nm light.

3.4. In vitro antibacterial effects

The antibacterial activities of NS1, NS2, NS3, and NS4 against *S. aureus* and *E. coli* was evaluated by the spread plate method with Ti being the control. Since the nanostructures possess intrinsic antibacterial ability, the antibacterial efficiency of the samples is first determined after incubation for 12 h in the absence of light. As shown in Fig. S8, the antibacterial ratios increase with surface roughness and NS4 shows the best killing efficiency of about 20% of *S. aureus* and *E. coli* suggesting overall weak antibacterial effects. The different TiO_2
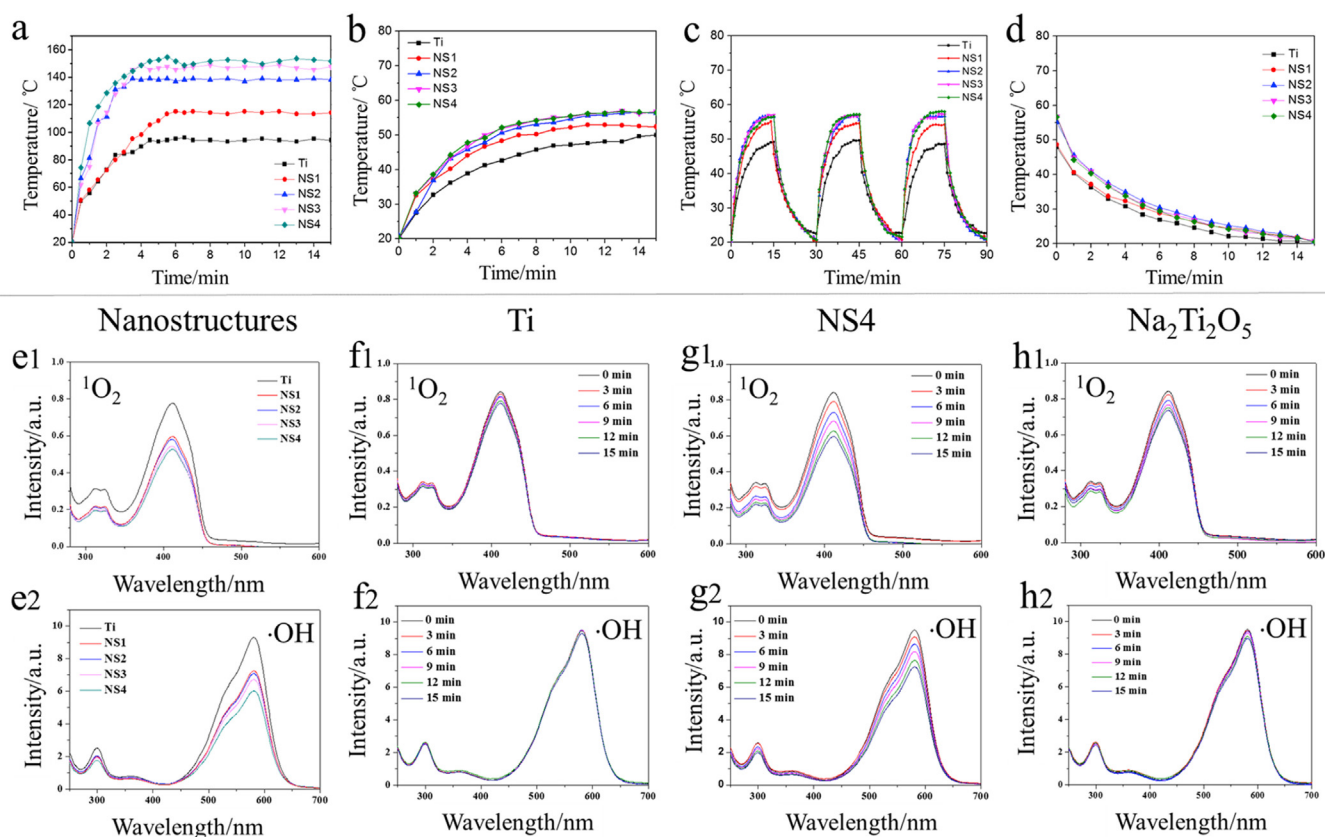
Fig. 2. Photothermal performance (a–d): (a) Temperature changes of TiO$_2$ nanostructures in air (power = 0.8 W cm^{-2}); (b) Temperature changes of the TiO$_2$ nanostructures in water (power = 0.8 W cm^{-2}); (c) Temperature rise and fall of the TiO$_2$ nanostructures in water when irradiation is turned on/off (power = 0.8 W cm^{-2}); (d) Cooling profiles of the TiO$_2$ nanostructures in PBS after turning off the laser (power = 0.8 W cm^{-2}). Detection of ROS upon irradiation with 808 NIR light at 0.8 W cm^{-2} for 15 min(e-h): (e1) $^1O_2$ and (e2) ·OH detected from the decay of DPBF and methyl violet of the TiO$_2$ nanostructures; (f1-h1) $^1O_2$ detected from the decay of DPBF of Ti, NS4 and Na$_2$Ti$_2$O$_5$ nanorod arrays upon irradiation at different time, respectively; (f2-h2) ·OH detected from the decay of methyl violet of Ti, NS4 and Na$_2$Ti$_2$O$_5$ nanorod arrays upon irradiation at different time, respectively.

nanostructures show different antibacterial efficiency under irradiation with 808 nm NIR light at various power densities. In general, the antibacterial properties of NS1, NS2, NS3, and NS4 increase gradually with increasing surface roughness under the same condition and NS4 with the molding nanorod structure exhibits the strongest antibacterial activity (Fig. 3a–d). Besides the surface roughness, the antibacterial efficiency increases with light power and time of irradiation. After irradiation with 0.6 W cm^{-2} for 15 min, the nanostructures exhibit poor antibacterial efficiency of less than 10% and 30% towards *S. aureus* and *E. coli*, respectively (Fig. 3a). This is related to the lower temperature produced by irradiation. However, when NS4 is irradiated with NIR light (0.8 W cm^{-2}), the antibacterial efficiency increases remarkably reaching 99% against both *S. aureus* and *E. coli*, meaning that NS4 can kill a significant amount of bacteria within 15 min (Fig. 3 b). When the power is increased to 1.0 W cm^{-2}, the maximum temperature reaches 59.5 °C (Fig. 3 c) and the antibacterial efficiency of NS4 is about 100% and 99.9% against *E. coli* and *S. aureus*, respectively, within 15 min. When the power is increased to 1.2 W cm^{-2}, the highest temperature is 64.1 °C, the antibacterial efficiency of NS2, NS3, and NS4 against both *S. aureus* and *E. coli* is approximately 100% (Fig. 3 d). In comparison, *E. coli* is more susceptible to the high temperature and nanostructured antibacterial platform than *S. aureus* due to the thinner membrane of Gram-negative bacteria [41,42].

The anti-biofilm properties of the nanostructures were determined under irradiation with 0.8 W cm^{-2} for 15 min (Fig. 3 f). For reference, Ti was cultured with the bacteria for the same period of time and served as the control. After culturing for 48 h, relative uniform and dense biofilms were formed on Ti but on the other hand, the TiO$_2$

nanostructures have excellent anti-biofilm ability. Abundance red fluorescence is observed from NS1 demonstrating the excellent anti-biofilm characteristics and the red spots on NS4 indicate that the bacteria have been killed almost completely.

The change in bacterial membrane permeability caused by Ti and NS4 was confirmed ONPG hydrolysis assays. As shown in Figure S 9a, there seems to be no discernible difference in the hydrolysis of ONPG between Ti and NS4 in the group of without light irradiation. However, NS4 exhibits increased hydrolysis of ONPG compared to Ti after irradiated with NIR light (0.8 W cm^{-2}) for 15 min, suggesting that the bacterial membrane permeability is improved obviously. The leakage of cellular components caused by Ti and NS4 was also investigated (Figure S 9b). The results of protein leakage show the same changing trends as that of ONPG hydrolysis, indicating that the combined actions of hyperthermia, ROS, and puncturing by the nanorod can kill bacteria efficiently.

3.5. Antibacterial mechanism

The nanostructures have excellent antibacterial properties especially against adhesive biofilms under the irradiation of 808 nm NIR light and the antibacterial mechanism may be attributed to the following mechanisms: (1) Hyperthermia produced by photothermal conversion; (2) ROS generated

By the TiO$_2$ nanostructures under light irradiation; (3) Physical puncture by the nanostructures. It is generally known that hyperthermia can kill bacteria. To verify the antibacterial properties of the TiO$_2$nanostructures under the irradiation of 808 light caused by the
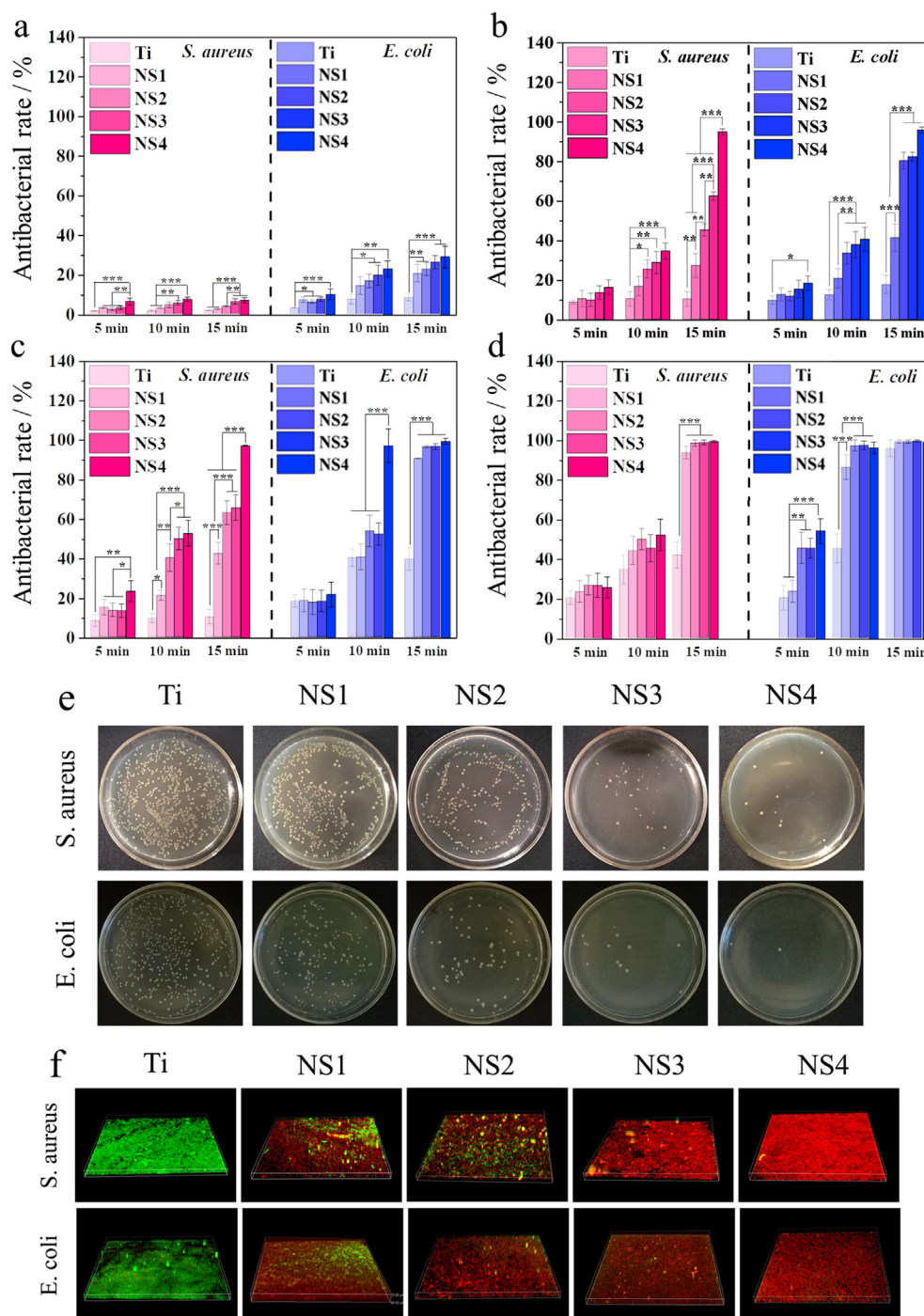
Fig. 3. Antibacterial performance: (a–d) Antibacterial rates of the Ti, NS1, NS2, NS3, and NS4 under irradiation with 808 nm NIR light at 0.6, 0.8, 1.0 and 1.2 W cm^{-2}, respectively; (e) Bacteria colony images ofthe different sample suponirradiation with 808 NIR light at 0.8 W cm^{-2} for 15 min; (f) Anti-biofilm performance of the different samples under irradiation with 808 NIR light at 0.8 W cm^{-2} for 15 min (*p < 0.05, **p < 0.01, ***p < 0.001).

synergistic effects and not just hyperthermia, the effect of temperature on *S. aureus* is thus investigated. As shown in Fig. S10, when the bacteria were incubated in an incubator at 65 °C for 15 min, only several bacteria colonies are observed from the plate of Ti, indicating that most of the bacteria can be killed at this temperature. However, many bacteria colonies can be observed from Ti at 60 °C for 15 min, and compared to Ti, the surface coverage on NS4 is lower, suggesting that bacteria can survive at 60 °C while the nanostructures exhibited antibacterial effects at this temperature in just 15 min. There is no significant difference in the bacteria number between Ti and NS4 at 55 °C, implying that the nanorods cannot kill bacteria at this temperature

within 15 min. However, under the irradiation with NIR light at 0.8 W cm^{-2}, the temperature of NS4 is near 55 °C, but NS4 exhibits excellent antibacterial activities in that condition. In addition to the antibacterial effects of nanostructures, these results also indirectly prove that ROS generated by the TiO$_2$ nanostructures play an important role in bacteria killing.

To further evaluate the effects of ROS on the antibacterial activity, 660 nm visible light was used to irradiate the TiO$_2$ nanostructures and ROS generation under irradiation with 660 nm visible light at 0.8 W cm^{-2} is presented in Fig. 4 a-b. 660 nm visible light can excite TiO$_2$ nanostructures to generate a certain amount of ^{1}O$_2$ and ·OH and
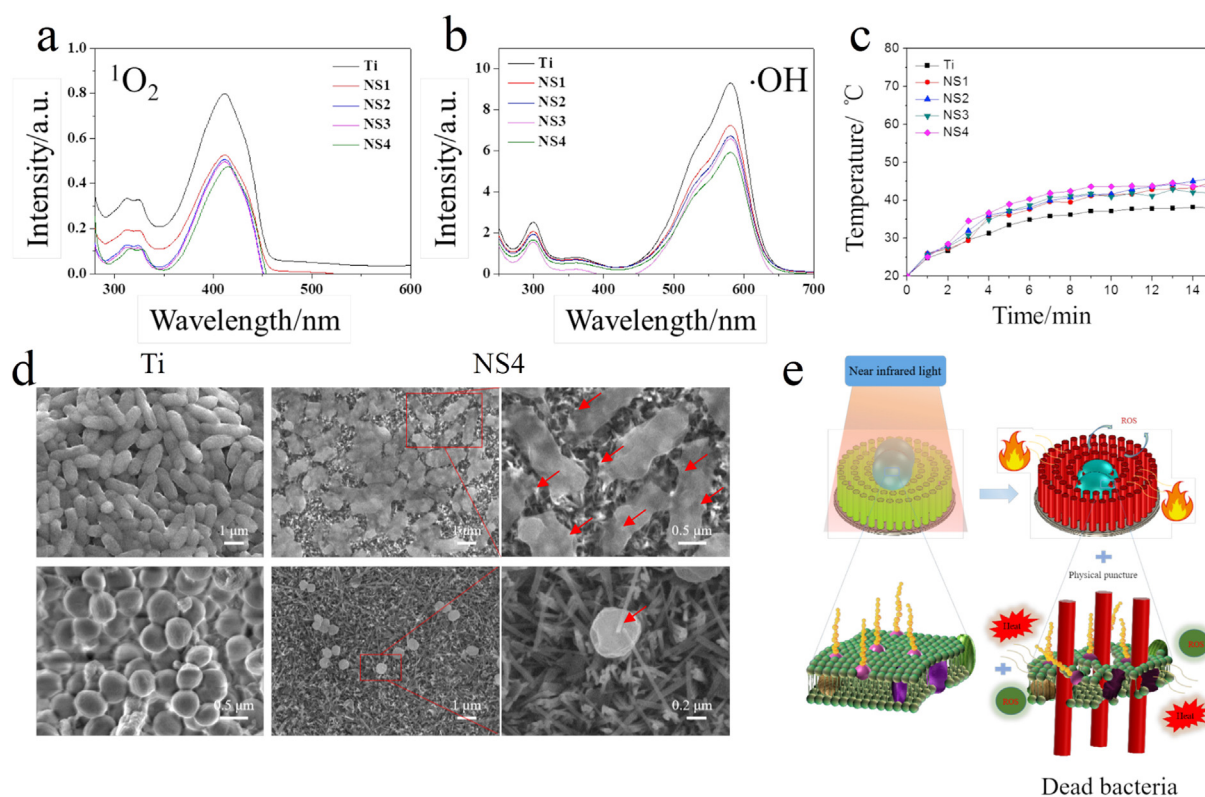
Fig. 4. (a) $^1O_2$ and (b) ·OH detected by the decay of DPBF and methyl violet under irradiation with 660 NIR at 0.8 W cm^{-2} for 15 min, respectively; (c) Temperature change of the TiO$_2$ nanostructures in air upon irradiation with 660 NIR at 0.8 W·cm^{-2}; (d) SEM images of *E. coli* and *S. aureus* on TiO$_2$ nanostructures upon irradiation with 808 NIR at 0.8 W cm^{-2} for 15 min; (e) Schematic illustration showing the antibacterial mechanism of the TiO$_2$ nanorod arrays under irradiation of 808 nm laser.

the yield shows little difference compared to that under irradiation with 808 nm NIR light showing decreased absorbance (Figure S 11). However, according to the heating curves of the samples in water (Fig. 4 c), the maximum temperature of the nanostructures is less than 45 ˚C. Under such conditions, the antibacterial activity against *S. aureus* is evaluated after illumination for 15 min and as shown in Figure S 12, NS1, NS2, NS3, and NS4 do not exhibit obvious antibacterial activity, suggesting that the generated ROS cannot kill *S. aureus* even in the presence of the nanostructures and temperature approaching 45 ˚C.

The TiO$_2$ nanostructures can generate a certain amount of ROS when exposed to 808 NIR light or 660 nm visible light and as aforementioned, the amount of ROS is small and cannot kill bacteria efficiently. Normally, a small amount of ROS exists in bacteria during normal aerobic respiration and it can cause a series of bacterial biological responses and be mitigated by antioxidant defense in the bacteria [43]. When the ROS produced in the solution reaches a certain level, they can work with the intracellular ROS to destroy the bacterial defense resulting in death [44]. However, an excess amount of ROS may cause cytotoxic effects resulting in cellular apoptosis [45–47]. The generated ROS produced by the TiO$_2$ nanorod arrays alone cannot kill bacteria and cause toxicity to cells but in combination with the generated heat and puncturing by the nanorods, biofilms are effectively eliminated.

In addition to the rising temperature and generated ROS, the bactericidal behavior is related to the nanopatterns [48,49]. According to related experiments, the antibacterial activity is directly related to the surface feature of the nanostructures such as the size, shape density, and rigidity of the nanostructures. In general, surfaces with tighter and smaller nanopillars are more effective in killing bacteria compared to lower density and larger nanopillars on the same surface [50,51]. In this work, the antibacterial activity of TiO$_2$ nanostructures show an increasing trend with surface roughness under the same conditions and

NS4 with the nanorod structure exhibits the strongest bactericidal activity.

To better understand the level of interaction between the nanostructure and bacterial cells, SEM was used to observe the *E. coli* and *S. aureus* biofilm formed on Ti and NS4 after irradiated with NIR light at 0.8 W·cm^{-2} for 15 min. The morphological appearance of all bacteria that attached to the surface of NS4 is significantly different to those attaching to Ti surface (Fig. 4 d). The cellular integrity is obvious disrupted by the nanostructures, and bacteria on NS4 is pulled on by the nanorods and collapsed around the nanostructure. The results confirm the findings of Ivanova [8], Yi [52], Kelleher [53] and Jenkins [54]. They investigated the bactericidal properties of different nanostructural features, and the morphological change of the dead bacteria is consistent with our findings. They were convinced that the nanostructure plays a major role in the bacteria-killing process and can induce deformation and penetration of the bacterial cell envelope. In addition, Jenkins proposed that TiO$_2$nanopillars also could trigger production of ROS within bacterial cells and increased abundance of oxidative stress proteins, the cumulative effects of which could impair bacterial growth and biofilm formation [54]. However, the number of bacteria inoculated on their samples is relatively little and culturing for a long time the nanostructure will exhibit bactericidal ability, while in this work only 15 min NS4 can exhibit excellent antibacterial ability under the irradiation with 808 NIR light. In addition, the morphologies of the dead bacteria mainly induced by the combination of PTA with PDA are different [19,24], which also demonstrated the importance of the nanostructure during the bacteria-killing.

Based on the experimental results, the antibacterial mechanism is proposed. As shown in Fig. 4e, the synergistic effects of the generated hyperthermia and ROS by the TiO$_2$ nanostructures during the irradiation with 808 nm NIR light increase the bacterial membrane permeability [55,56] and the combined actions of hyperthermia, ROS, and
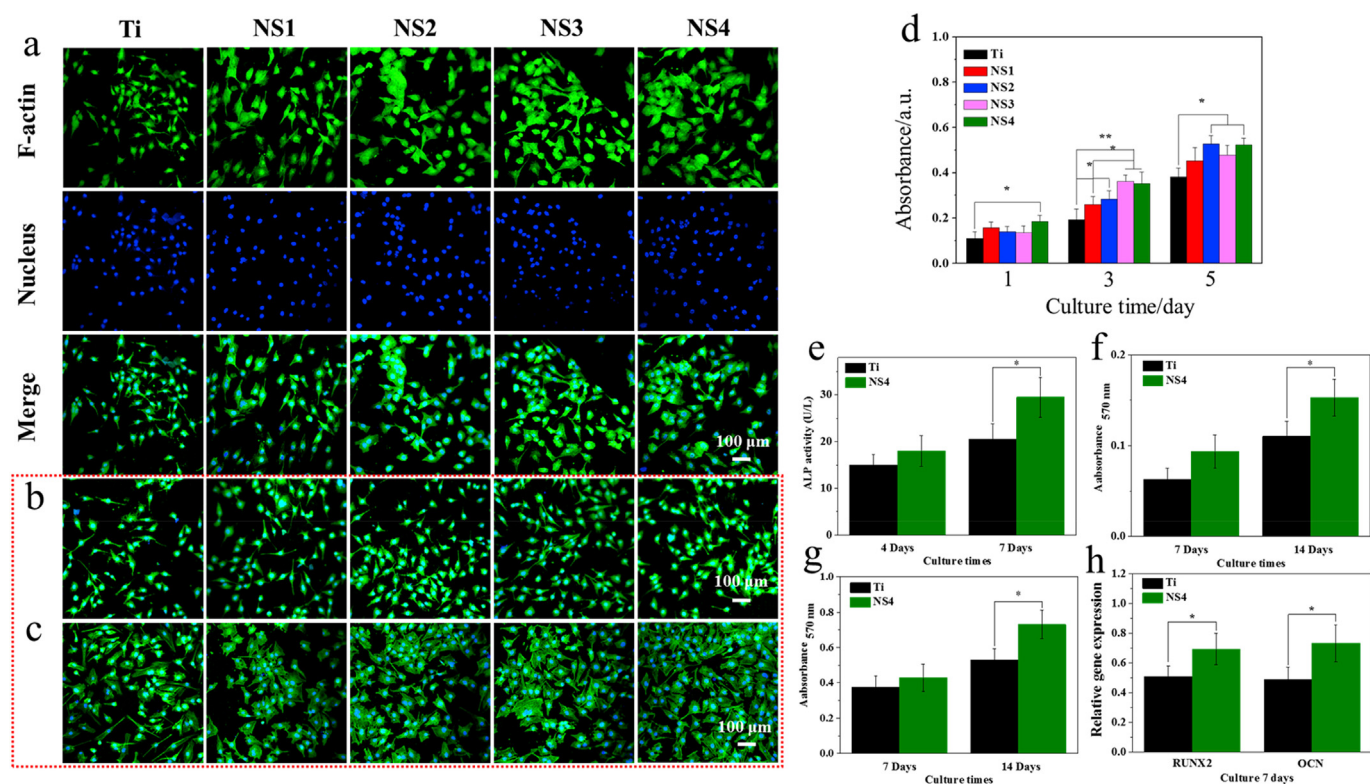
Fig. 5. Biological assessment: (a) Fluorescence images of MC3T3-E1 osteoblasts cultured on Ti, NS1, NS2, NS3, and NS4 for 24 h; (b) Fluorescence images of MC3T3-E1 osteoblasts after irradiation with 808 NIR light at 0.8 W cm^{-2} for 15 min; (c) Fluorescence images of NIR light irradiated MC3T3-E1 osteoblasts after re-culturing for 24 h; (d) Cell proliferation measured by MTT after culturing for 1, 3, and 5 days; (e) Quantitative ALP activity; (f) Collagen secretion; (g) ECM mineralization of MC3T3-E1 on Ti and NS4 on the 4th and 7th day; (h) Osteogenisis-related genes RUNX2 and OCN expressions on Ti and NS4 (*p < 0.05, **p < 0.01).

puncturing by the nanorod disrupt the cell membranes causing leakage of cytoplasmic contents and eventual bacterial death [57,58].

3.6. Biocompatibility assessment

Besides the antibacterial properties, biocompatibility is of vital importance for biomedical implants. Fig. 5 a shows the cell morphology and spreading activity of MC3T3-E1 osteoblasts on the samples after fluorescent staining. After culturing for 24 h, most of the osteoblasts retain the spherical shape but spread poorly on Ti, whereas those on the TiO$_2$ nanostructures have a polygonal shape with a large number of filopodia and lamellipodia, suggesting that the nanostructures promoted cell spreading. It has been shown that a nanopatterned surface can improve adhesion, spreading, and differentiation of osteoblasts and the potential mechanism is mediated by cell alignment of the cytoskeleton and formation of focal adhesions [59–62]. To investigate the effects of light irradiation, the cells on the samples were irradiated with the 808 nm NIR light at 0.8 W cm^{-2} for 15 min and the cell morphology was examined and shown in Fig. 5 b. The osteoblasts on Ti exhibit no difference in terms of viability and morphology compared to those without light irradiation. However, after light irradiation, the cells on the TiO$_2$ nanostructures are slightly atrophic. This phenomenon may be due to the synergistic effects of the generated hyperthermia and ROS on the TiO$_2$ nanostructures. The cells on the samples are further cultured for 24 h to investigate the lasting effects of light irradiation. The MC3T3-E1 osteoblasts spread well on all the samples, especially NS4 (Fig. 5 c). The biocompatibility of the samples was also assessed by the MTT assay. As shown in Fig. 7d, the TiO$_2$ nanostructures promoted MC3T3-E1 osteoblasts proliferation on Ti. The ALP activity, collagen secretion, and ECM mineralization of Ti and NS4 were determined to investigate osteogenic differentiation after culturing for 4 and 7 days (Fig. 5 e − 5 g) and the TiO$_2$ nanorod arrays improved osteogenic

differentiation slightly. The osteoblast-related gene expressions of the RUNX2 and OCN on Ti and NS4 are measured using the RT-QPCR. The TiO$_2$ nanorod arrays promoted the expression of RUNX2 and OCN slightly compared to Ti (Fig. 5 h) further demonstrating that irradiation with NIR light causes negligible side effects to the cell behavior.

The TiO$_2$ nanostructures without light irradiation exhibit the intrinsic antibacterial ability and at the same time, promote proliferation, spreading, and differentiation of osteoblasts. This is because bacteria and mammalian cells attach to and sense biomaterials differently. Attachment of bacteria to the implant surface and subsequently breeding depend on the formation of a community within the extracellular polymeric substance, while eukaryotic cells can adhere to the implant surface as single cells mediated by integrins and focal adhesions [63,64]. Nanopatterns have been shown to promote the expression of integrins and formation of focal adhesions consequently promoting assembly of the cytoskeletal structure [65]. Although light irradiation inhibits the cell viability due to the synergistic effect of the generated hyperthermia and ROS on the TiO$_2$ nanostructures, the osteoblasts spread well on all the TiO$_2$ nanostructures after additional culturing for 24 h.

3.7. Antibacterial assay in vivo

Based on the *in vitro* results, NS4 was selected for the *in vivo* study with Ti serving as the control. Two subcutaneous *S. aureus* infection models including common bacterial infection and biofilm infection using mice were adopted first. The four groups were irradiated with the 808 nm laser at the implanted site for 15 min. Considering the effects of hyperthermia on the mice, the maximum temperature was controlled to about 50 °C to avoid scalding injury, and the *in vivo* temperature changes recorded by a thermal camera are shown in Figure S 13. The *in vitro* antibacterial property of NS4 is first investigated under the
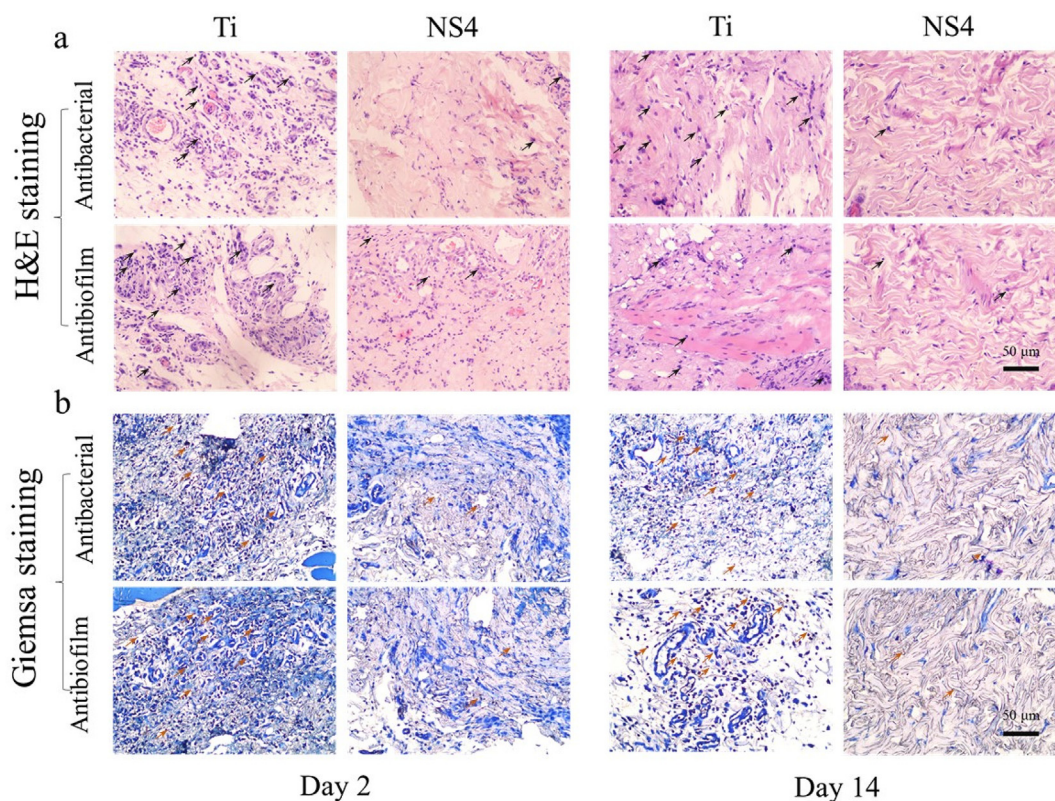
Fig. 6. *In vivo* antibacterial assessment: (a) H&E and (b) Giemsa staining images of the tissues at the 2nd and 14th day showing the degree of tissue infection in mice treated with Ti and NS4 and irradiated with 808 NIR for 15 min.

lighting conditions, and NS4 exhibits excellent antibacterial activity (Figure S 14). To determine the antibacterial activity *in vivo*, the spread plate method is implemented. On the 2nd day post-implantation, the samples were removed and subjected to ultrasonic vibration to isolate the surface bacteria. The bacteria solution was spread on agar plates and incubated at 37 °C for 24 h.

The results are shown in Figure S 15. Many bacteria survive on the Ti group, especially the biofilm-infected Ti group, but only several bacterial colonies can be found from both the bacterial and biofilm-infected NS4 group.

Giemsa staining and H&E staining were performed to evaluate bacterial infection of the soft tissues surrounding the implant after irradiation for 2 and 14 days as shown in Fig. 6. After Giemsa staining, numerous lymphocytesare observed from the Ti group on the 2nd day, especially the biofilm-infected Ti group. However, the number of lymphocytes decreases significantly in both the bacterial and biofilm-infected NS4 groups. After 14 days, there are still a lot of lymphocytes in the Ti group but inflammation has basically subsided for the NS4 group. Although the bacteria are smaller than the lymphocytes and many bacteria are covered by lymphocytes, numerous bacteria are observed from the corresponding slices of the Ti group. In contrast, a small number of bacteria are found from the NS4 group and after 14 days, few bacteria can be found. Similarly, the typical feature of soft tissue infection appears from the Ti group after H&E staining. That is, a lot of lymphocytes and a few inflammatory cells are observed but on the other hand,the NS4 group shows milder inflammation with fewer lymphocytes. After 14 days, the inflammatory reaction is reduced in the Ti group and few lymphocytes can be found from the NS4 group. The results indicate that the TiO$_2$ nanorod arrays under irradiation with 808 NIR light produce excellent antibacterial activity *in vivo* and also can eradicate the attached biofilms on the implant surface.

3.8. Osteogenic activity in vivo

We further evaluated the antibiofilm performance and osteogenic activity of NS4 on Ti rod *in vivo*. Ti and NS4 adhered by biofilms implants were implanted in the tibia to develop implant-associated infective rat model. The morphology of the nanorod arrays on Ti rod implants is the same as that of on Ti plate (Figure S 16). After suturing the wounds, the implantation sites in the two groups were irradiated with 808 NIR light for 15 min and the highest temperature was controlled to about 50 °C. As shown in Fig. 7 a and Fig. 7 b, the temperature of both Ti and NS4 gradually rises within 8 min, then finally stabilized at about 40 and 50 °C, respectively. After raising for two days, the rods were removed, rolled on agar petri dishes and then soaked in culture mediums. The petri dishes and culture mediums were photographed after further incubated at 37 °C for 24 h (Fig. 7c and d). For the Ti group, a multitude of bacterial colonies are observed on culture plates and the culture mediums are turbid. However, only several bacterial colonies are found on the plates corresponding to NS4 and the culture mediums are very clear. The antibacterial efficiency of NS4 is calculated to be 95.7% relative to that of Ti. These results indicate that the bacterial biofilm established on NS4 was substantially eradicated with NIR light irradiation *in vivo*. The results of H&E staining (Fig. 7 e) and Giemsa staining (Fig. 7 f) of the tissues from the implants are consistent with that of the subcutaneous models. A large number of lymphocytes (indicated by black arrows) are observed in the Ti implant group, suggesting acute inflammation, while fewer inflammatory cells are found in the NS4 group after NIR light irradiation. In addition, there are a lot of bacteria (marked by brown arrows) in the Ti group. However, fewer adherent bacteria are observed in the tissues around the NS4 implant, indicating that the inflammation response can be significantly suppressed by the synergistic effects of hyperthermia, ROS and physical rupturing of the TiO$_2$ nanorod arrays.

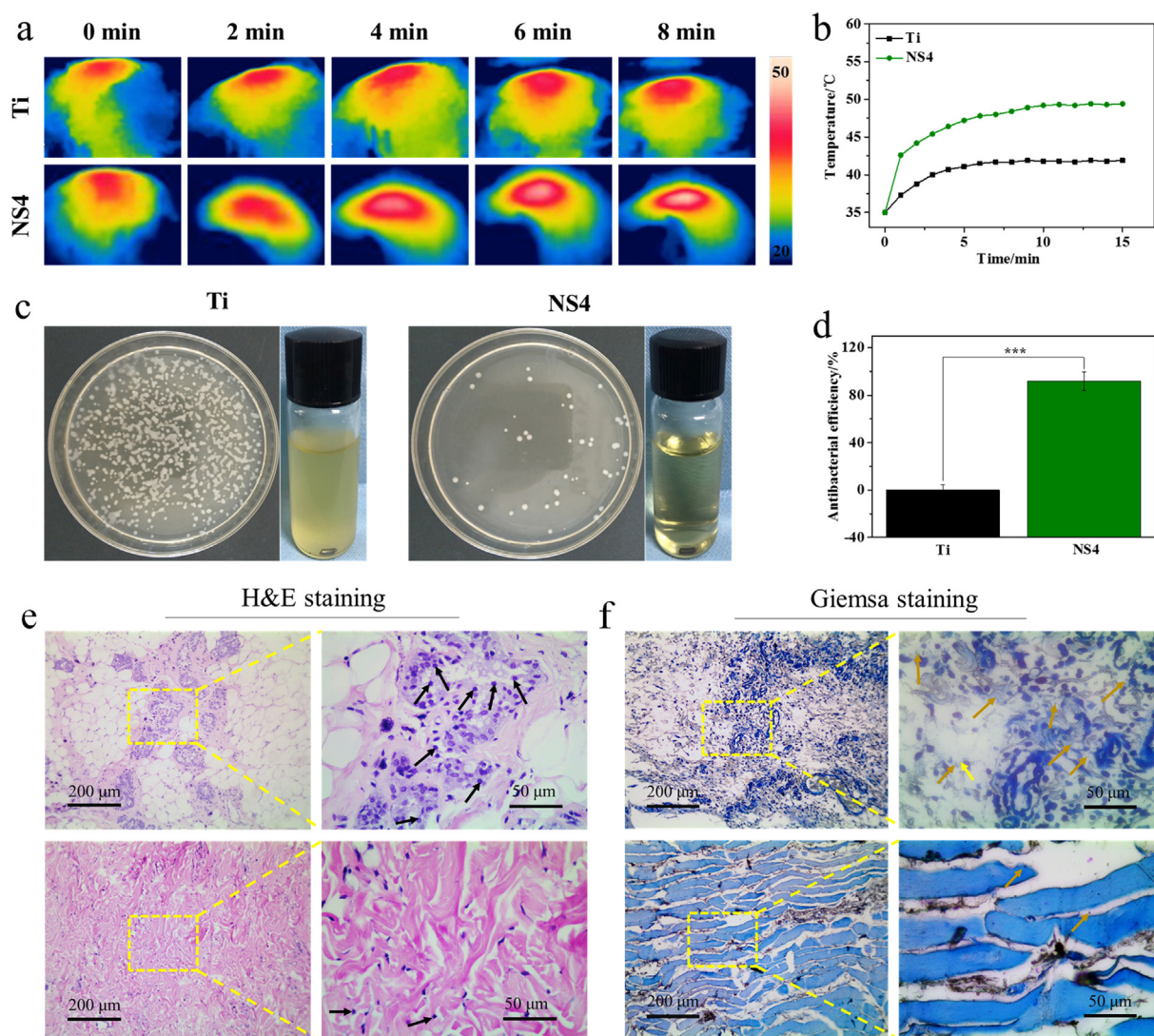After one month of implantation, the newly formed bone on Ti and

Fig. 7. (a) Thermal images and (b) temperature changes of Ti and NS4 under 808 nm light irradiation *in vivo*; (c) Photograph of bacteria colonies and culture mediums of Ti and NS4 rods taken from mice; (d) The corresponding antibacterial efficiency *in vivo*. (***p < 0.001); (e) H&E and (f) Giemsa staining of the bone tissue around the Ti and NS4 implants.

NS4 after the irradiation of NIR light were monitored by micro-CT. The new bone formation is observed clearly by the reconstructed 3Dimages (Fig. 8 a and Fig. 8 b), and the new bone mass in the NS4 group is much greater than that of the Ti group. The Quantitative analysis (Fig. 8 c) suggests that the corresponding bone volume/tissue volume (Obj.V/TV) of Ti and NS4 is 22.39 and 40.47, respectively. Fig. 8 b1–b3 show the 2D micro-CT images of NS4 implant group in tibia from different directions. The osteogenic or cartilage differentiation around the Ti and NS4 was evaluated by Safranin-O/Fast Green staining. The cartilage and new formed bone can be stained with red and green, respectively. As shown in Fig. 8 d, more green section formed in the NS4 group, suggesting that the osteogenic differentiation around the NS4 is higher than that of around the Ti implant. Moreover, Methylene Blue−Acid Fuchsin was also used to analyze the new bone formation, and the new formed bone can be stained into red. Fig. 8 e shows that the new bone formed in the NS4 group is significantly higher than that of the Ti group. The increased amount of new bone on NS4 group in the presence of *S.aureus* is attributed to aspects: (1) The disinfection of the NS4 implant under NIR light irradiation by the synergistic effects of physical-chemical mechanism improved the osseointegration; (2) The TiO$_2$ nanorod arrays on implants promoted the osteogenic behavior of osteoblasts, thereby enhancing new bone formation.

It has been shown that NIR light triggered PTA requires a high temperature to induce protein disruption and bacteria death but the excessive temperature or long-time irradiation may cause burns and heat injury to the surrounding tissues [66,67]. In this work, the maximum temperature is controlled to be less than 50 °C and the irradiation time to 15 min. Hence, light irradiation does not damage the tissues around the implants *in vivo* but combined with puncturing by the nanorods, excellent antibacterial activity and eradication of biofilms are accomplished. In addition, the TiO$_2$ nanostructures on implants promoted the osteogenic behavior of osteoblasts, thereby promoting the new bone formation, and some bone growth factors such as arginine–glycine–aspartic acid–cysteine can be immobilized on the surface of the nanostructures to further promoteosteogenesis and osseointegration [19,24].

4. Conclusion

In conclusion, we have established a multiple synergetic antibacterial modality by TiO$_2$ nanostructures under the irradiation of 808 nm NIR light. The system are demonstrated to have excellent antibiofilm effect *in vitro* and *in vivo*. The antibacterial mechanism arises from synergistic effects of hyperthermia and ROS generated by the TiO$_2$
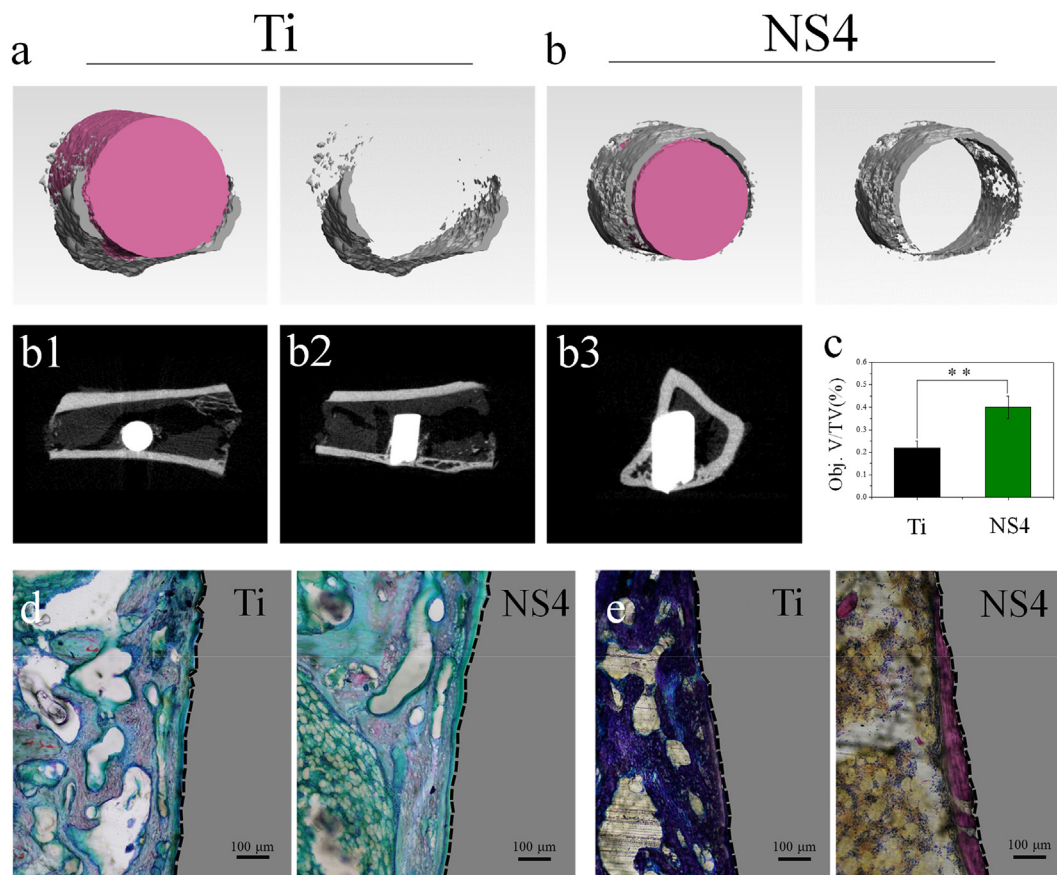
Fig. 8. *In vivo* osteogenic performance: (a, b) 3D images reconstructed by micro-CT in Ti and NS4 implants; (b1-b3) 2D micro-CT images of NS4implants in tibia; (c) Quantitative analysis of bone volume/total volume (BV/TV) around the implants calculated from the micro-CT(**p < 0.01); (d) Safranin-O/Fast Green staining of the tissue around the implantsafter 1month implantation; (e) Methylene Blue-Acid Fuchsin staining of the tissue around the implantsafter 1month implantation.

nanostructures and physical rupturing induced by the nanostructures. The nontoxic TiO$_2$ nanostructures also promote proliferation, spreading, and differentiation of osteoblasts in the presence of NIR light irradiation. Moreover, the implant with TiO$_2$ nanostructures effectively improve new bone formation even in an infected micro environment *in vivo* under NIR light irradiation. This work reveals a practical strategy for highly efficient bacteria killing and single specie biofilm eradication *in vivo* consequently mitigating potential bacteria-related complications after surgery. The system with a multiple antimicrobial mechanism is expected to be a promising approach with high biosafety to avoid the side effects arising from single modality.

Declaration of competing interest

There are no conflicts to declare.

Appendix A. Supplementary data

Supplementary data to this article can be found online at https://doi.org/10.1016/j.bioactmat.2020.07.017.

References

[1] C.R. Arciola, D. Campoccia, L. Montanaro, Implant infections: adhesion, biofilm formation and immune evasion, Nat. Rev. Microbiol. 16 (2018) 397–409.
[2] W. Cassandra, The drug-resistant bacteria that pose the greatest health threats, Nature 543 (2017) 15.
[3] D. Li, Y.H. Li, A. Shrestha, S. Wang, Q.Q. Wu, L.J. Li, C. Guan, C. Wang, T.W. Fu, W.Z. Liu, Y.D. Huang, P. Ji, T. Chen, Effects of programmed local delivery from a micro/nano- hierarchical surface on titanium implant on infection clearance and osteogenic induction in an infected bone defect, Adv. Healthcare Mater. (2019) 1900002.
[4] X.K. Shen, Y.Y. Zhang, P.P. Ma, L. Sutrisno, Z. Luo, Y. Hu, Y.L. Yu, B.L. Tao, C.Q. Li, K.Y. Cai, Fabrication of magnesium/zinc-metal organic framework on titanium implants to inhibit bacterial infection and promote bone regeneration, Biomaterials 212 (2019) 1–16.
[5] L. Zhang, J.Q. Guo, X.Y. Huang, Y.N. Zhang, Y. Han, The dual function of Cu-doped TiO$_2$ coatings on titanium for application in percutaneous implants, J. Mater. Chem. B 4 (2016) 3788–3800.
[6] A. Gao, R.Q. Hang, X.B. Huang, L.Z. Zhao, X.Y. Zhang, L. Wang, B. Tang, S.L. Ma, P.K. Chu, The effects of titania nanotubes with embedded silver oxide nanoparticles on bacteria and osteoblasts, Biomaterials 35 (2014) 4223–4235.
[7] H.M.C. de Azeredo, Antimicrobial nanostructures in food packaging, Trends Food Sci. Technol. 30 (2013) 56–69.
[8] E.P. Ivanova, J. Hasan, H.K. Webb, G. Gervinskas, S. Juodkazis, V.K. Truong, A.H.F. Wu, R.N. Lamb, V.A. Baulin, G.S. Watson, J.A. Watson, D.E. Mainwaring, R.J. Crawford, Bactericidal activity of black silicon, Nat. Commun. 4 (2013) 2838.
[9] M. Michalska, F. Gambacorta, R. Divan, I.S. Aranson, A. Sokolov, P. Noirota, P.D. Laible, Tuning antimicrobial properties of biomimetic nanopatterned surfaces, Nanoscale 10 (2018) 6639–6650.
[10] K. Modaresifar, S. Azizian, M. Ganjian, L.E. Fratila-Apachitei, A.A. Zadpoor, Bactericidal effects of nanopatterns: a systematic review, Acta Biomater. 83 (2019) 29–36.

[11] A. Susarrey-Arce, I. Sorzabal-Bellido, A. Okniańska, F. McBride, A.J. Beckett, J.G.E. Gardeniers, R. Raval, R.M. Tiggelaar, Y.A. Diaz Fernandez, Bacterial viability on chemically modified silicon nanowire arrays, J. Mater. Chem. B 4 (2016) 3104–3112.

[12] A. Gupta, S. Mumtaz, C.H. Li, I. Hussain, V.M. Rotello, Combatting antibiotic-resistant bacteria using nanomaterials, Chem. Soc. Rev. 48 (2019) 415–427.

[13] E.P. Ivanova, J. Hasan, H.K. Webb, V.K. Truong, G.S. Watson, J.A. Watson, V.A. Baulin, S. Pogodin, J.Y. Wang, M.J. Tobin, C. Löbbe, R.J. Crawford, Natural bactericidal surfaces: mechanical rupture of Pseudomonas aeruginosa by cicada wings, Small 8 (2012) 2489–2494.

[14] J. Hasan, H.K. Webb, V.K. Truong, S. Pogodin, V.A. Baulin, G.S. Watson, J.A. Watson, R.J. Crawford, E.P. Ivanova, Selective bactericidal activity of nano-patterned super hydrophobic cicada Psaltoda claripennis wing surfaces, Appl. Microbiol. Biotechnol. 97 (2013) 9257–9262.

[15] Q. Yu, J. Cho, P. Shivapooja, L.K. Ista, G.P. López, Nanopatterned smart polymer surfaces for controlled attachment, killing, and release of bacteria, ACS Appl. Mater. Interfaces 5 (2013) 9295–9304.

[16] M.L. Yin, Z.H. Li, E.G. Ju, Z.Z. Wang, K. Dong, J.S. Ren, X.G. Qu, Multifunctional upconverting nanoparticles for near-infrared triggered and synergistic antibacterial resistance therapy, Chem. Commun. 50 (2014) 10488–10490.

[17] M. Pandurangan, G. Enkhtaivan, D.H. Kim, Cytotoxic effects of aspartame on human cervical carcinoma cells, Toxicol. Res. 5 (2016) 45–52.

[18] Y. Qiao, F. Ma, C. Liu, B. Zhou, Q.L. Wei, W.L. Li, D.N. Zhong, Y.Y. Li, M. Zhou, Near-infrared laser-excited nanoparticles to eradicate multidrug-resistant bacteria and promote wound healing, ACS Appl. Mater. Interfaces 10 (2018) 193–206.

[19] L. Tan, J. Li, X.M. Liu, Z.D. Cui, X.J. Yang, S.L. Zhu, Z.Y. Li, X.B. Yuan, Y.F. Zheng, K.W.K. Yeung, H.B. Pan, X.B. Wang, S.L. Wu, Rapid biofilm eradication on bone implants using red phosphorus and near-infrared light, Adv. Mater. 30 (2018) 1801808.

[20] M.L. Yin, Z.H. Li, E.G. Ju, Z.Z. Wang, K. Dong, J.S. Ren, X.G. Qu, Multifunctional upconverting nanoparticles for near-infrared triggered and synergistic antibacterial resistance therapy, Chem. Commun. 50 (2014) 10488.

[21] W. Li, J.S. Wang, J.S. Ren, X.G. Qu, 3D graphene oxide–polymer hydrogel: near-infrared light-triggered active scaffold for reversible cell capture and on-demand release, Adv. Mater. 25 (2013) 6737–6743.

[22] L. Tan, J. Li, X.M. Liu, Z.D. Cui, X.J. Yang, K.W.K. Yeung, H.B. Pan, Y.F. Zheng, X.B. Wang, S.L. Wu, In situ disinfection through photoinspired radical oxygen species storage and thermal-triggered release from black phosphorous with strengthened chemical stability, Small 14 (2018) 1703197.

[23] Q. Gao, X. Zhang, W.Y. Yin, D.Q. Ma, C.J. Xie, L.R. Zheng, X.H. Dong, L.Q. Mei, J. Yu, C.Z. Wang, Z.J. Gu, Y.L. Zhao, Functionalized MoS₂ nanovehicle with near-infrared laser-mediated nitric oxide release and photothermal activities for advanced bacteria-infected wound therapy, Small 14 (2018) 1802290.

[24] M. Li, L.Q. Li, K. Su, X.M. Liu, T.J. Zhang, Y.Q. Liang, D.D. Jing, X.J. Yang, D. Zheng, Z.D. Cui, Z.Y. Li, S.L. Zhu, K.W.K. Yeung, Y.F. Zheng, X.B. Wang, S.L. Wu, Highly efficient and noninvasive near-infrared eradication of a Staphylococcus aureus biofilm on implants by a photo responsive coating within 20 min, Adv. Sci. (2019) 1900599.

[25] Z. Yuan, B.L. Tao, Y. He, J. Liu, C.C. Lin, X.K. Shen, Y. Ding, Y.L. Yu, C.Y. Mu, P. Liu, K.Y. Cai, Biocompatible MoS₂/PDA-RGD coating on titanium implant with anti-bacterial property via intrinsic ROS-independent oxidative stress and NIR irradiation, Biomaterials 217 (2019) 119290.

[26] X.J. Cheng, R. Sun, L. Yin, Z.F. Chai, H.B. Shi, M.Y. Gao, Light-triggered assembly of gold nanoparticles for photothermal therapy and photoacoustic imaging of tumors in vivo, Adv. Mater. 29 (2017) 1604894.

[27] X.R. Deng, K. Li, X.C. Cai, B. Liu, Y. Wei, K.R. Deng, Z.X. Xie, Z.J. Wu, P.A. Ma, Z.Y. Hou, Z.Y. Cheng, J. Lin, A hollow-structured CuS@Cu₂S@Au nanohybrid: synergistically enhanced photothermal efficiency and photo switchable targeting effect for cancer theranostics, Adv. Mater. 29 (2017) 1701266.

[28] S.L. Wu, Z.Y. Weng, X.M. Liu, K.W.K. Yeung, P.K. Chu, Functionalized TiO₂ based nanomaterials for biomedical applications, Adv. Funct. Mater. 24 (2014) 5464–5481.

[29] N. Wei, H.Z. Cui, Q. Song, L.Q. Zhang, X.J. Song, K. Wang, Y.F. Zhang, J. Li, J. Wen, J. Tian, Ag₂O nanoparticle/TiO₂ nanobelt heterostructures with remarkable photo-response and photocatalytic properties under UV, visible and near-infrared irradiation, Appl. Catal. B Environ. 198 (2016) 83–90.

[30] J.Y. Liao, B.X. Lei, H.Y. Chen, D.B. Kuang, C.Y. Su, Oriented hierarchical single crystalline anatase TiO₂ nanowire arrays on Ti-foil substrate for efficient flexible dye-sensitized solar cells, Energy Environ. Sci. 5 (2012) 5750–5757.

[31] X.D. Wang, Z.D. Li, J. Shi, Y.H. Yu, One-dimensional titanium dioxide nanomaterials: nanowires, nanorods, and nanobelts, Chem. Rev. 114 (2014) 9346–9384.

[32] J.Y. Liao, D. Higgins, G. Lui, V. Chabot, X.C. Xiao, Z.W. Chen, Multifunctional TiO₂−C/MnO₂ core−double−shell nanowire arrays as high-performance 3D electrodes for lithium ion batteries, Nano Lett. 13 (2013) 5467–5473.

[33] X.S. Peng, A.C. Chen, Large-scale synthesis and characterization of TiO₂-based nanostructures on Ti substrates, Adv. Funct. Mater. 16 (2006) 1355–1362.

[34] J. Li, X.M. Liu, L. Tan, Y.Q. Liang, Z.D. Cui, X.J. Yang, S.L. Zhu, Z.Y. Li, Y.F. Zheng, K.W.K. Yeung, X.B. Wang, S.L. Wu, Light-activated rapid disinfection by accelerated charge transfer in red phosphorus/ZnO heterointerface, Small Methods 3 (2019) 1900048.

[35] W.T. Dang, T. Li, B. Li, H.S. Ma, D. Zhai, X.C. Wang, J. Chang, Y. Xiao, J.W. Wang, C.T. Wu, A bifunctional scaffold with CuFeSe₂ nanocrystals for tumor therapy and bone reconstruction, Biomaterials 160 (2018) 92–106.

[36] T. Csizmadia, M. Erdélyi, T. Smausz, T. Novák, B. Hopp, Simulation of the reflectivity properties of microstructured titanium surface by ray tracing method, J. Laser Micro Nanoen. 10 (2015) 210–215.

[37] X.J. Gong, X.F. Gao, L. Jiang, Recent progress in bionic condensate microdrop self-propelling surfaces, Adv. Mater. 29 (2017) 1703002.

[38] J. Zhu, Y.T. Luo, J. Tian, J. Li, X.F. Gao, Clustered ribbed-nanoneedle structured copper surfaces with high-efficiency dropwise condensation heat transfer performance, ACS Appl. Mater. Interfaces 7 (2015) 10660–10665.

[39] Z.Z. Feng, X.M. Liu, L. Tan, Z.D. Cui, X.J. Yang, Z.Y. Li, Y.F. Zheng, K.W.K. Yeung, S.L. Wu, Electrophoretic deposited stable chitosan@MoS₂ coating with rapid in situ bacteria-killing ability under dual-light irradiation, Small 14 (2018) 1704347.

[40] X.Y. Zhang, C. Zhang, Y.Q. Yang, H.Y. Zhang, X.B. Huang, R.Q. Hang, X.H. Yao, Light-assisted rapid sterilization by a hydrogel incorporated with Ag₃PO₄/MoS₂ composites for efficient wound disinfection, Chem. Eng. J. 374 (2019) 596–604.

[41] H.J. Busscher, R.J.B. Dijkstra, E. Engels, D.E. Langworthy, D.I. Collias, D.W. Bjorkquist, M.D. Mitchell, H.C. van der Mei, Removal of two waterborne pathogenic bacterial strains by activated carbon particles prior to and after charge modification, Environ. Sci. Technol. 40 (2006) 6799–6804.

[42] H.M. Yadav, S.V. Otaria, R.A. Bohara, S.S. Mali, S.H. Pawar, S.D. Delekar, Synthesis and visible light photocatalytic antibacterial activity of nickel-doped TiO₂ nanoparticles against Gram-positive and Gram-negative bacteria, J.Photoch.Photobio. A. 294 (2014) 130–136.

[43] G.M. Wang, H.Q. Feng, L.S. Hu, W.H. Jin, Q. Hao, A. Gao, X. Peng, W. Li, K.Y. Wong, H.Y. Wang, Z. Li, P.K. Chu, An antibacterial platform based on capacitive carbon-doped TiO₂ nanotubes after direct or alternating current charging, Nat. Commun. 9 (2018) 2055.

[44] G.M. Wang, W.H. Jin, A.M. Qasim, A. Gao, X. Peng, W. Li, H.Q. Feng, P.K. Chu, Antibacterial effects of titanium embedded with silver nanoparticles based on electron-transfer-induced reactive oxygen species, Biomaterials 124 (2017) 25–34.

[45] M.V.D.Z. Park, A.M. Neigh, J.P. Vermeulen, L.J.J. de la Fonteyne, H.W. Verharen, J.J. Briedé, H. van Loveren, W.H. de Jong, The effect of particle size on the cytotoxicity, inflammation, developmental toxicity and genotoxicity of silver nanoparticles, Biomaterials 32 (2011) 9810–9817.

[46] H. Wu, J. Lin, P.D. Liu, Z.H. Huang, P. Zhao, H.Z. Jin, J. Ma, L.P. Wen, N. Gu, Reactive oxygen species acts as executor in radiation enhancement and autophagy inducing by AgNPs, Biomaterials 101 (2016) 1–9.

[47] J. Ahmad, H.A. Alhadlaq, M.A. Siddiqui, Q. Saquib, A.A. Al-Khedhairy, J. Musarrat, M. Ahamed, Concentration-dependent induction of reactive oxygen species, cell cycle arrest and apoptosis in human liver cells after nickel nanoparticles exposure, Environ. Toxicol. 30 (2015) 137–148.

[48] L.E. Fisher, Y. Yang, M.F. Yuen, W. Zhang, A.H. Nobbs, B. Su, Bactericidal activity of biomimetic diamond nanocone surfaces, Biointerphases 11 (2016) 011014.

[49] W. Wang, T.L. Li, H.M. Wong, P.K. Chu, R.Y. Kao, S. Wu, F.K. Leung, T.M. Wong, M.K. To, K.M. Cheung, Development of novel implants with self-antibacterial performance through in-situ growth of 1D ZnO nanowire, Colloids Surf., B 141 (2016) 623–633.

[50] D.P. Linklater, H.K.D. Nguyen, C.M. Bhadra, S. Juodkazis, E.P. Ivanova, Influence of nanoscale topology on bactericidal efficiency of black silicon surfaces, Nanotechnology 28 (2017) 245301.

[51] A. Elbourne, R.J. Crawford, E.P. Ivanova, Nano-structured antimicrobial surfaces: from nature to synthetic analogues, J. Colloid Interface Sci. 508 (2017) 603–616.

[52] G.S. Yi, Y. Yuan, X.K. Li, Y.G. Zhang, ZnO nanopillar coated surfaces with substrate-dependent superbactericidal property, Small 14 (2018) 1703159.

[53] S.M. Kelleher, O. Habimana, J. Lawler, B. O' Reilly, S. Daniels, E. Casey, A. Cowley, Cicada Wing Surface Topography: an investigation into the bactericidal properties of nanostructural features, ACS Appl. Mater. Interfaces 8 (2016) 14966–14974.

[54] J. Jenkins, J. Mantell, C. Neal, A. Gholinia, P. Verkade, A.H. Nobbs, B. Su, Antibacterial effects of nanopillar surfaces are mediated by cell impedance, penetration and induction of oxidative stress, Nat. Commun. 11 (2020) 1626.

[55] Y. Li, X.M. Liu, L. Tan, Z.D. Cui, D.D. Jing, X.J. Yang, Y.Q. Liang, Z.Y. Li, S.L. Zhu, Y.F. Zheng, K.W.K. Yeung, D. Zheng, X.B. Wang, S.L. Wu, Eradicating multidrug-resistant bacteria rapidly using a multi functional g-C₃N₄@ Bi₂S₃ nanorod heterojunction with or without antibiotics, Adv. Funct. Mater. 29 (2019) 1900946.

[56] C.Y. Mao, Y.M. Xiang, X.M. Liu, Y.F. Zheng, K.W.K. Yeung, Z.D. Cui, X.J. Yang, Z.Y. Li, Y.Q. Liang, S.L. Zhu, S.L. Wu, Local Photothermal/photodynamic synergistic therapy by disrupting bacterial membrane to accelerate reactive oxygen species permeation and protein leakage, ACS Appl. Mater. Interfaces 11 (2019) 17902–17914.

[57] C.Y. Mao, Y.M. Xiang, X.M. Liu, Z.D. Cui, X.J. Yang, Z.Y. Li, S.L. Zhu, Y.F. Zheng, K.W.K. Yeung, S.L. Wu, Repeatable photodynamic therapy with triggered signaling pathways of fibroblast cell proliferation and differentiation to promote bacteria-accompanied wound healing, ACS Nano 12 (2018) 1747–1759.

[58] X.H. Wang, K. Su, L. Tan, X.M. Liu, Z.D. Cui, D.D. Jing, X.J. Yang, Y.Q. Liang, Z.Y. Li, S.L. Zhu, K.W.K. Yeung, D. Zheng, S.L. Wu, Rapid and highly effective noninvasive disinfection by hybrid Ag/CS@MnO₂ nanosheets using near-infrared light, ACS Appl. Mater. Interfaces 11 (2019) 15014–15027.

[59] L. Richert, F. Vetrone, J.H. Yi, S.F. Zalzal, J.D. Wuest, F. Rosei, A. Nanci, Surface nanopatterning to control cell growth, Adv. Mater. 20 (2008) 1488–1492.

[60] V.V.D. Rani, L. Vinoth-Kumar, V.C. Anitha, K. Manzoor, M. Deepthy, V.N. Shantikumar, Osteointegration of titanium implant is sensitive to specific nanostructure morphology, Acta Biomater. 8 (2012) 1976–1989.

[61] X.L. Liu, S.T. Wang, Three-dimensional nano-biointerface as a new platform for guiding cell fate, Chem. Soc. Rev. 43 (2014) 2385–2401.

[62] R.A. Gittens, R. Olivares-Navarrete, Z. Schwartz, B.D. Boyan, Implant osseointegration and the role of microroughness and nanostructures: lessons for spine implants, Acta Biomater. 10 (2014) 3363–3371.

[63] K. Anselme, P. Davidson, A. Popa, M. Giazzon, M. Liley, L. Ploux, The interaction of cells and bacteria with surfaces structured at the nanometre scale, Acta Biomater. 6 (2010) 3824–3846.

[64] Y. Sun, C.S. Chen, J. Fu, Forcing stem cells to behave: a biophysical perspective of the cellular microenvironment, Annu. Rev. Biophys. 41 (2012) 519–542.

[65] K.S. Brammer, C. Choi, C.J. Frandsen, S. Oh, S. Jin, Hydrophobic nanopillars initiate mesenchymal stem cell aggregation and osteo-differentiation, Acta Biomater. 7 (2011) 683–690.

[66] D.W. Yoo, H.Y. Jeong, S.H. Noh, J.H. Lee, J.W. Cheon, Magnetically triggered dual functional nanoparticles for resistance free apoptotic hyperthermia, Angew. Chem. Int. Ed. 52 (2013) 13047–13051.

[67] Y. Yang, W.J. Zhu, Z.L. Dong, Y. Chao, L. Xu, M.W. Chen, Z. Liu, 1D coordination polymer nanofibers for low-temperature photothermal therapy, Adv. Mater. 29 (2017) 1703588.